Supplementary Information for
Magnetic skyrmion lattice disclinations in pentagon- and heptagon-shaped FeGe nanostructures

Thibaud Denneulin[1], Nikolai S. Kiselev[2], Vladyslav M. Kuchkin[3], Rafal E. Dunin-Borkowski[1]

[1] *Ernst Ruska-Centre for Microscopy and Spectroscopy with Electrons, Forschungszentrum Jülich, 52425 Jülich, Germany.*

[2] *Peter Grünberg Institute and Institute for Advanced Simulation, Forschungszentrum Jülich and JARA, 52425 Jülich, Germany.*

[3] *Department of Physics and Materials Science, University of Luxembourg, L-1511 Luxembourg.*

Supplementary Information 1: Sample preparation of pentagon and heptagon geometries using focused ion beam

Figure S1 illustrates the method used to prepare pentagon and heptagon-shaped samples using a scanning electron microscope and Ga^+ focused ion beam (FIB-SEM) machine. A lift-out procedure is first performed to extract a piece of sample from a bulk crystal [1]. A $\sim 10 \times 2 \times 2$ µm^3 layer of carbon is deposited locally to protect the surface of the sample (a,b) using electron beam-induced and ion beam-induced deposition (EBID and IBID). The area around the deposit is then milled (c) to free a piece of sample of approximately $10 \times 2 \times 5$ µm^3. The piece of sample is extracted using a micro-probe (d) and attached to a 3 mm copper grid (e) again using IBID of carbon. After the probe is released, the surfaces of the sample can be polished and flattened, which is recommended for the next step. The sample is then flipped 90° so that it is perpendicular to the ion beam for patterning the desired geometry (g), in this case a pentagon. A 30 kV and 80 pA Ga^+ ion beam was used for this step. The milling duration should not be too long so that it does not completely pass through the sample. However, it should be long enough to reach approximately 500 nm deep so that surface damage layers can be removed later. The milling duration can be calibrated by sacrificing a small region of the sample to check how much time is needed to go through. After patterning, the milled regions are filled with carbon using IBID and the same pattern as for milling (h). The sample is then flipped back to its original orientation to thin it down to a thickness of approximately 150 nm. The backside of the sample (the patterned side is considered as the front side) is first milled until the pattern becomes visible (j,k) in SEM. Finally, the front side can then be polished to remove surface damage created during the previous steps (l). Fig. S1(m,n) shows, for example, side-view and top-view SEM images of a TEM lamella patterned with pentagons of different sizes.

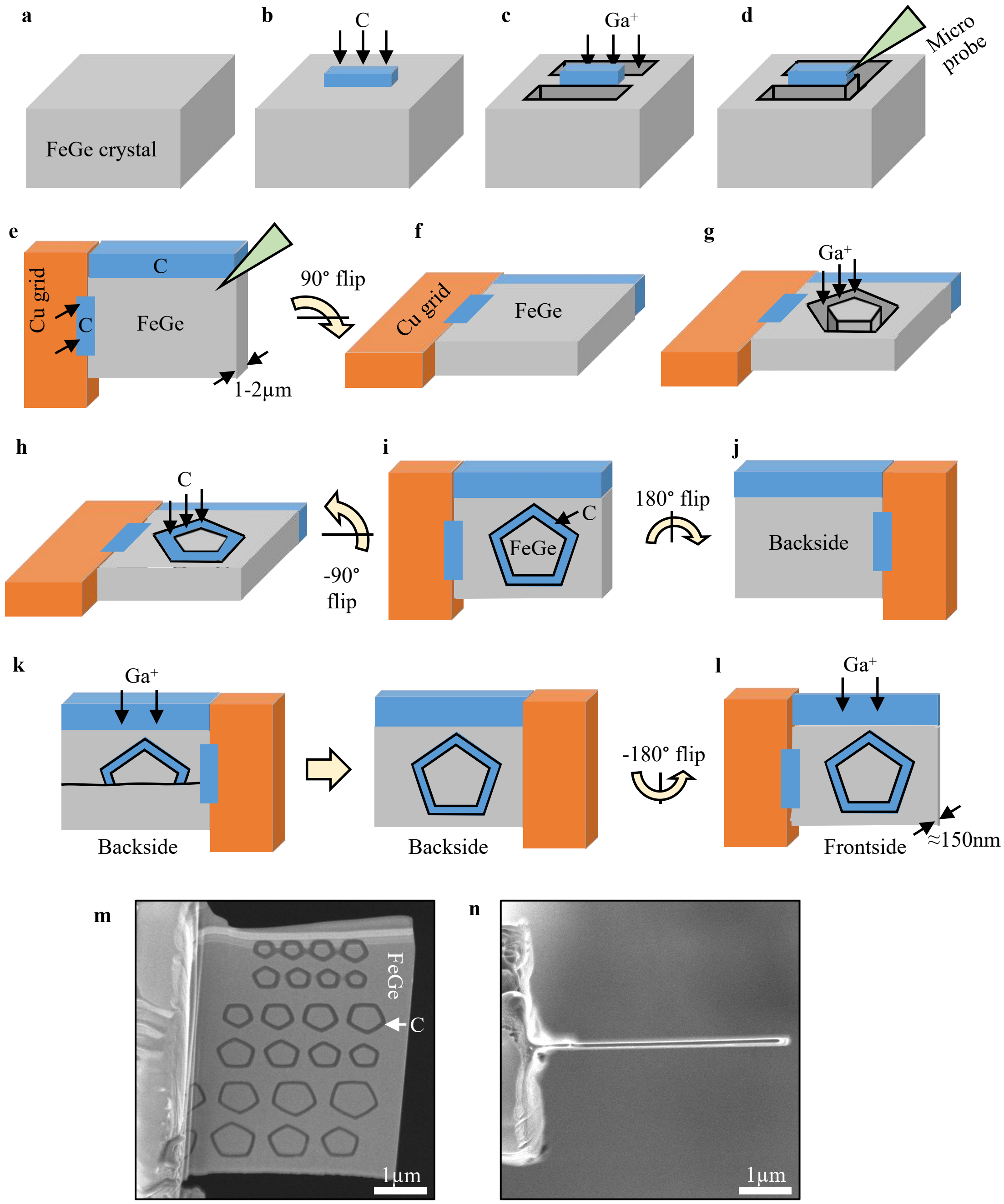

Figure S1: **FIB preparation of a TEM lamella with pentagon-shaped patterns.** (a) Bulk FeGe crystal. (b) Deposit a capping layer of carbon using EBID and IBID. (c) Mill areas around the capping layer. (d) Attach a micro-probe to the sample and free the remaining parts. (e) Attach the sample to a copper grid. (f) Flip the sample 90° around a horizontal axis. (g) Pattern the surface of the sample. (h) Deposit carbon in the patterned areas. (i) Flip the sample back to 0°. (j) Rotate the sample 180° around a vertical axis to expose the backside. (k) Mill the backside until the pattern becomes visible. (l) Rotate the sample back to 0° and thin it down to electron transparency. (m,n) Side-view and top-view SEM images of an example of a lamella patterned with pentagons of different sizes.

Supplementary Information 2: Applied field series of pentagon- and heptagon-shaped samples

Figure S2(a,b) shows Fresnel images of pentagon- and heptagon-shaped samples. The images were obtained at 220 K and in the presence of different external magnetic fields indicated in the figure. It shows the evolution of the magnetic domain structure from the helical state at low fields to the skyrmion lattice state at approximately 200 mT and then a saturated monodomain state at approximately 400 mT.

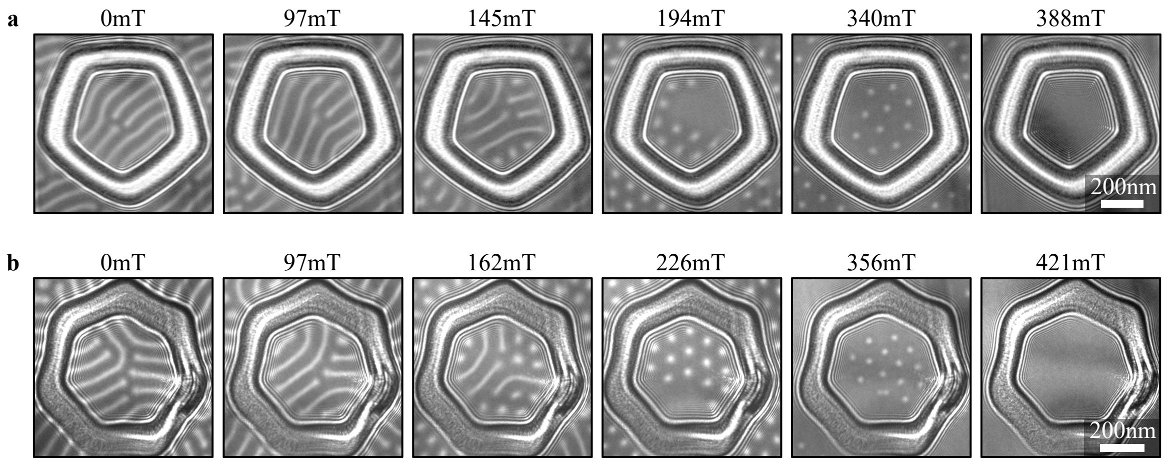

Figure S2: **LTEM applied field series**. (a) Fresnel image of a pentagon-shaped sample recorded at 220 K with a defocus of 500 µm and in the presence of different external magnetic fields indicated in the figure. (b) Same description in the case of a heptagon-shaped sample.

Supplementary Information 3: Skyrmion lattices in a heptagon-shaped sample

Figure S3(a) shows a TEM image of a heptagon-shaped sample with a side length of $l = 240$ nm. As shown schematically in Fig. S3(b), the total number of skyrmions in a 7-fold disclination state is

$$S = 1 + \sum_{n=1}^{N} 7n \,, \tag{S1}$$

with, in this case, $N = 2$ skyrmion rings and $S = 22$. Figure S3(c) shows Fresnel images of lattices with different skyrmion numbers obtained at 220 K and with an external magnetic field of 240 mT. In the 7-fold disclination with $S = 22$, the central skyrmion $n = 0$ has seven neighbors and the skyrmions of the inner ring $n = 1$ have six neighbors as shown schematically in Fig. S3(d). Interestingly, when $S = 21$, two skyrmions are removed from the outer ring $n = 2$ and one is added at the center $n = 0$. Therefore, the lattice shows two interconnected pentagons at the center. When $S = 20$, one skyrmion is removed from the center with respect to $S = 21$, forming again a heptagon at the center with two pentagons on the sides. On the other hand, when $S = 23$, one skyrmion is added to $n = 0$ with respect to $S = 22$ forming two pentagons at the center and two heptagons on the sides. These observations are in agreement with micromagnetic simulations shown in Fig. S3(e).

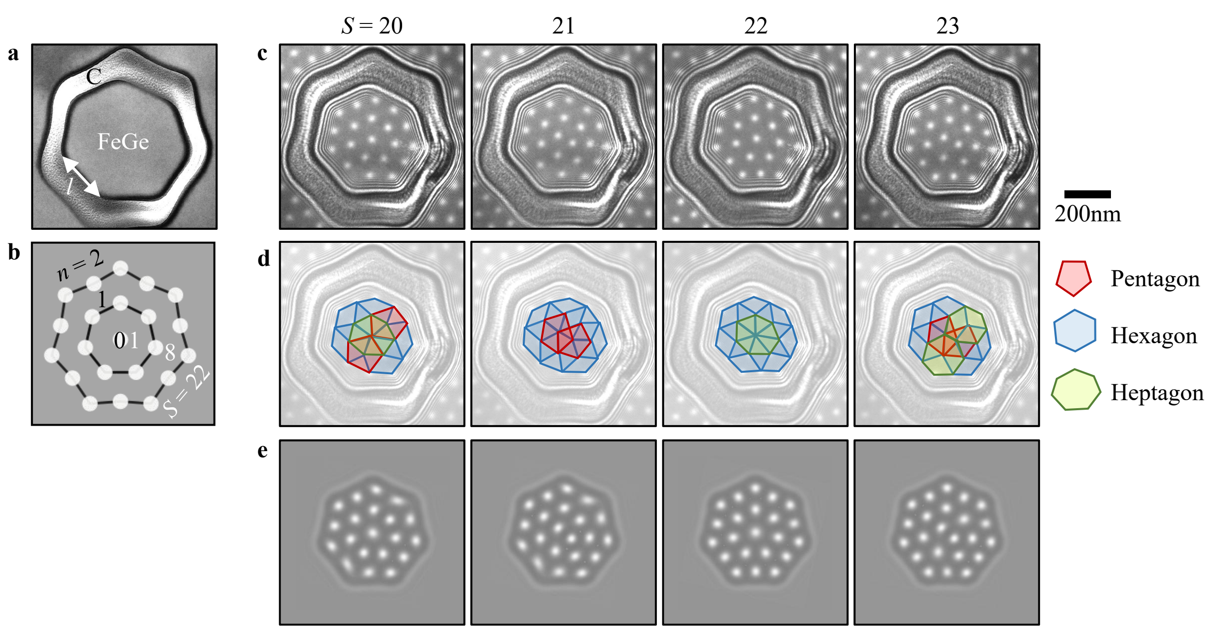

Figure S3: **LTEM of skyrmion lattices in a heptagon-shaped sample.** (a) In-focus TEM image of a heptagon-shaped sample with a side length of $l = 240$ nm. (b) Schematic showing a 7-fold disclination with 22 skyrmions. (c) Experimental Fresnel images obtained at 220 K with a defocus of 500 µm and in the presence of an external magnetic field of 240 mT. The images contain lattices with different skyrmion numbers indicated in the figure. (d) Previous images overlaid with pentagons, hexagons and heptagons. (e) Fresnel images calculated from micromagnetic simulations.

Supplementary Information 4: Magnetic and structural analysis of a 7-fold disclination

Figure S4(a) shows an off-axis electron hologram of the heptagon-shaped sample that hosts a 7-fold disclination. Fig. S4(b-e) shows the reconstructed magnetic phase image ϕ_{mag}, the magnitude and direction of the in-plane magnetic induction field $\boldsymbol{B}_{\perp}$, and profiles extracted from the phase image as indicated by the solid and dashed lines. It can be observed in (c,d) that the central skyrmion is slightly larger than the surrounding skyrmions. The profiles in (e) show that the interskyrmion distance d_r and skyrmion diameter $\varnothing_r$ along the radial direction (solid red profile) are larger than the corresponding distances d_t and $\varnothing_t$ along the tangential direction (dashed blue profile). The addition of a $2\pi/7$ wedge induces a compression of the seven wedges along the circular direction around the disclination. Figure S4(f-j) shows corresponding micromagnetic simulations and Table 1 reports the mean interskyrmion distances $(\overline{d_r}, \overline{d_t})$ and skyrmion diameters $(\overline{\varnothing_r}, \overline{\varnothing_t})$ of the experimental and simulated disclinations, which were found to be in good quantitative agreement.

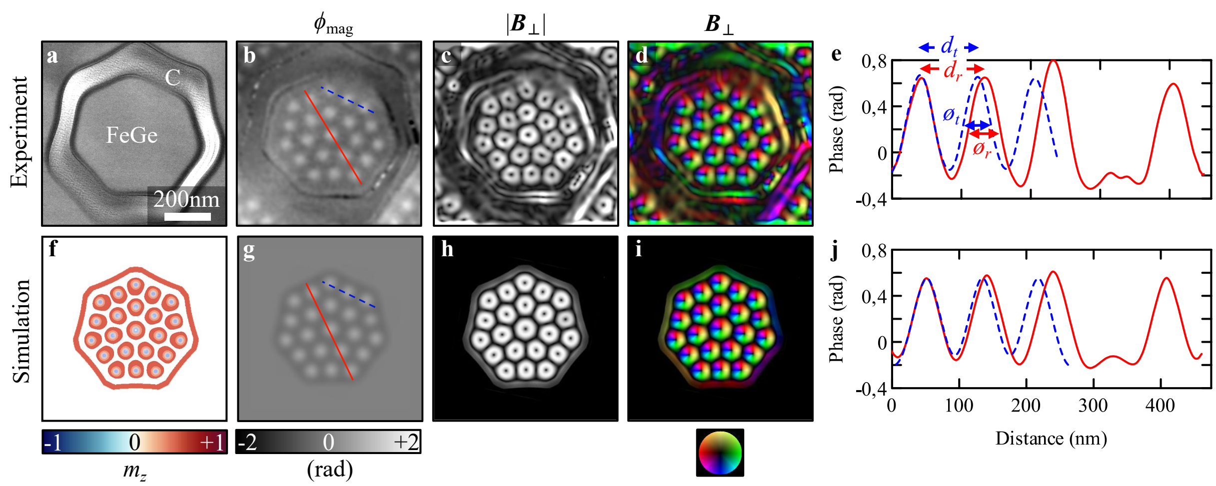

Figure S4: **Electron holography of a 7-fold disclination.** (a) Electron hologram of a heptagon-shaped sample recorded with an external magnetic field of 240 mT. (b) Magnetic phase image ϕ_{mag} obtained using off-axis electron holography. (c) Magnitude of the in-plane magnetic induction field $|\boldsymbol{B}_{\perp}|$. (d) Corresponding color-coded map showing the direction of $\boldsymbol{B}_{\perp}$. (e) Phase profiles extracted from (b) along the solid and dashed lines. (f) Isosurface representation of the normalized out-plane component m_z of a magnetization model calculated using micromagnetic simulation. (g-j) Corresponding phase image, magnetic field maps and profiles.

	$\overline{d_t}$	$\overline{d_r}$	$\overline{\varnothing_t}$	$\overline{\varnothing_r}$
Experiment (nm, ±2 nm)	83	95	42	44
Simulation (nm)	84	94	42	45
Ratio Exp. / Sim.	0.99	1.01	1.00	0.98

Table 1: **Skyrmion distances and diameters.** Mean interskyrmion distances $\overline{d}$ and skyrmion diameters $\overline{\varnothing}$ along the tangential t and radial r directions of the experimental and simulated disclinations. Ratios of experimental and simulated values are also reported.

To investigate the structure of the disclination in more detail, the coordinates of the skyrmions in the phase image shown in Fig. S5(a) were determined by calculating their center of mass. The local orientational parameter of the 7 hexagons was then calculated, as explained in the main article. Figures S5(b) and (c) represent respectively the orientation θ of the hexagons and their degree of hexagonality $|\Psi_6|$. The orientation θ changes by steps of approximately 9° along the circular direction and on average the hexagonality is $\langle|\Psi_6|\rangle = 0.85$. For comparison, the white dots in Fig. S5(d) show a 7-fold disclination model created from a hexagonal lattice (black dots) using linear elastic theory. Figure S5(e) and (f) show the corresponding rotation and hexagonality maps calculated from the positions in (d). The rotation changes by $\Delta\theta \approx 9°$ along the circular direction and the hexagonality is $|\Psi_6| = 0.91$, which is close to the experimental values.

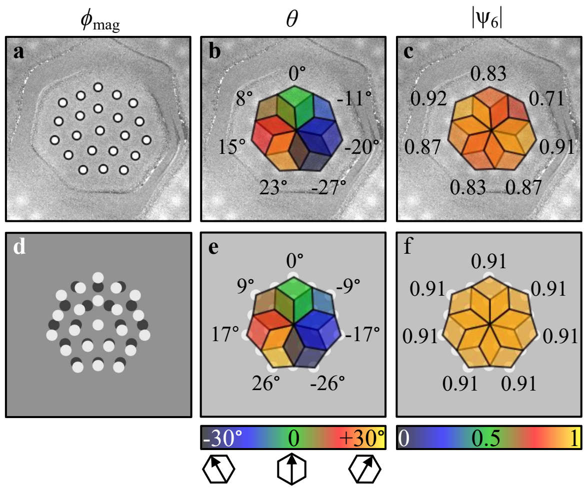

Figure S5: **Structural analysis and linear elastic theory.** (a) Position of the skyrmions in the magnetic phase image. (b) Orientation θ and (c) hexagonality $|\Psi_6|$ maps calculated from the positions in (a). (d) 7-fold disclination model calculated using linear elastic theory. (e) Corresponding orientation and (f) hexagonality maps.

Supplementary Information 5: Field evolution of a 5-fold disclination

Figure S6(a) shows an applied field series of magnetic phase images ϕ_{mag} of a 5-fold disclination in a pentagon-shaped sample. Figure S6(b,c) shows the corresponding magnitude and direction of the magnetic induction field $\boldsymbol{B}_{\perp}$. At low field, for instance 176 mT, the central skyrmion shows a pentagon shape and the surrounding skyrmions show a hexagonal shape that can be elongated along the circular direction around the disclination. When increasing the field, the skyrmions appear progressively smaller and more rounded. Figure S6(d) shows the mean tangential $\overline{\varnothing_t}$ and radial $\overline{\varnothing_r}$ skyrmion diameters as a function of the applied field. The ellipticity, defined as the $\overline{\varnothing_t}/\overline{\varnothing_r}$ ratio, is also plotted in Fig. S6(e). Both the tangential and radial diameters decrease with the applied magnetic field. However, the tangential diameter decreases faster, which also leads to a decrease of the ellipticity. The ellipticity varies between 1.34 and 1.06 over the applied field range of 176 mT to 278 mT. Finally, Fig. S6(f) shows the mean interskyrmion distances $\overline{d_t}$ and $\overline{d_r}$ along the tangential and radial directions. $\overline{d_t}$ is larger than $\overline{d_r}$ due to the disclination strain and both distances remain relatively stable as a function of the applied magnetic field.

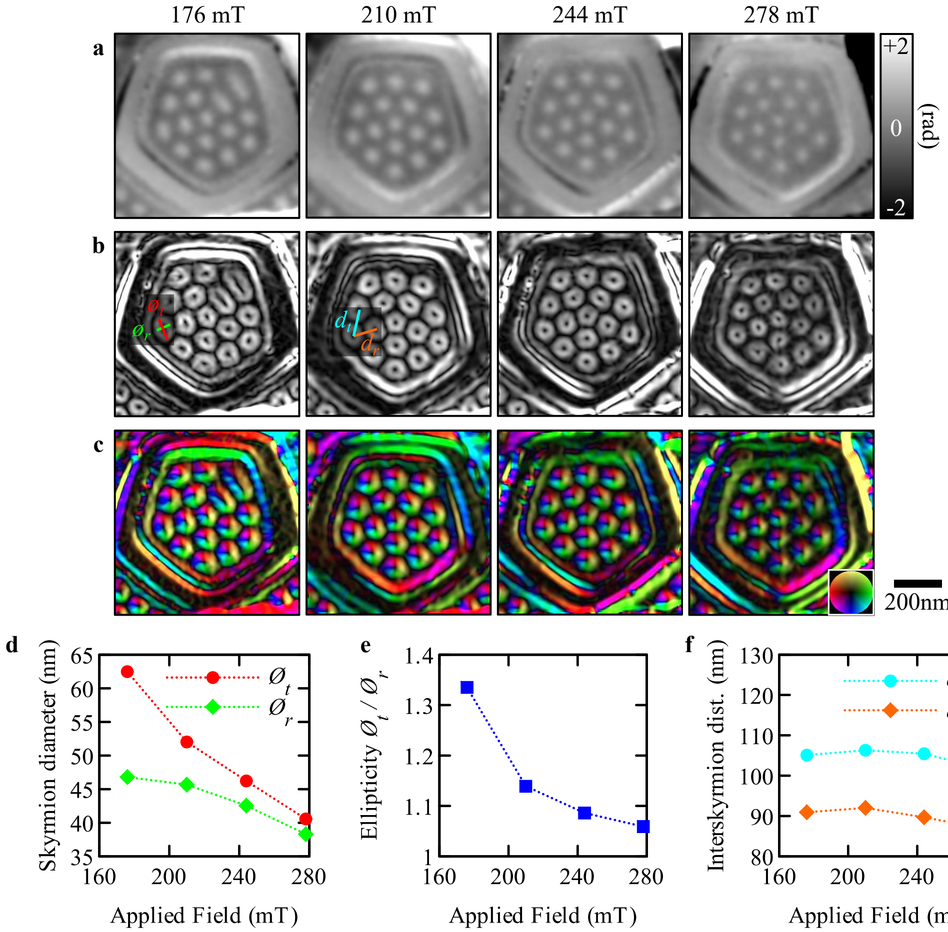

Figure S6: **Applied magnetic field series of a 5-fold disclination.** (a) Magnetic phase images ϕ_{mag} of a pentagon-shaped sample obtained at 220 K and with different external magnetic fields indicated in the figure. (b) Magnitude of the in-plane magnetic induction field $|\boldsymbol{B}_{\perp}|$. (c) Corresponding color-coded maps showing the direction of $\boldsymbol{B}_{\perp}$. (d) Mean tangential $\overline{\varnothing_t}$ and radial $\overline{\varnothing_r}$ skyrmion diameters for the different applied magnetic fields. (e) Corresponding ellipticity ratio $\overline{\varnothing_t}/\overline{\varnothing_r}$. (f) Mean tangential $\overline{d_t}$ and radial $\overline{d_r}$ interskyrmion distances.

Supplementary Information 6: Disclinations in pentagons and heptagons of different sizes

Figure S7(a-c) shows experimental LTEM images obtained in pentagons of increasing sizes that contain disclinations with (a) $N = 1$, (b) 2 and (c) 3 skyrmion rings. Figure S7(d-f) shows heptagons that contain the corresponding 7-fold disclinations. In practice, the probability to obtain large disclinations through field cycling is low and a large number of attempts were needed to obtain the disclinations with $N = 3$ rings.

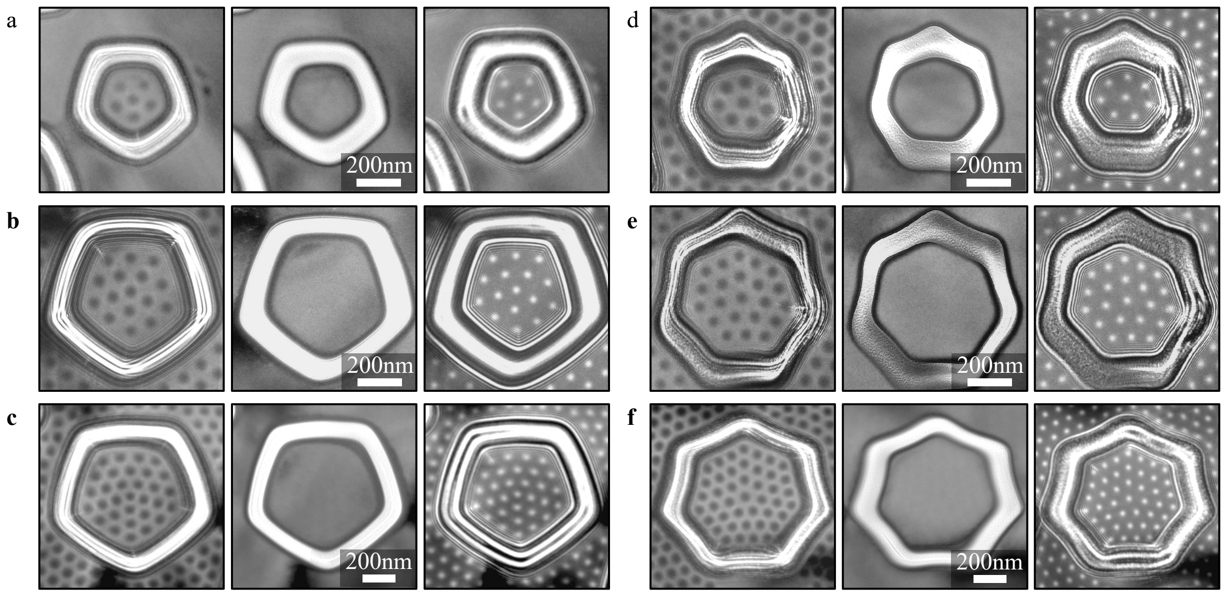

Figure S7: **LTEM imaging of skyrmion lattices in pentagon- and heptagon-shaped samples of different sizes.** (a-c) Pentagons that host 5-fold disclinations with $N = 1$ to 3 skyrmion rings observed at −500, 0, and +500 µm defocus. (d-f) Same description with heptagons that host 7-fold disclinations.

Supplementary Information 7: Skyrmion mobility around a disclination

It was observed in the main article that when $S = 17$ skyrmions in a pentagon, a 5-7 dislocation is created. The 7-coordinated skyrmion of the dislocation can be located in any of the five different corners of the pentagon leading to five geometrically and energetically equivalent configurations. It is possible to switch between the different configurations by tilting the sample with respect to the applied out-of-plane magnetic field and so adding a small in-plane component to it. Figure S8(a) shows a similar situation but with a larger pentagon that contains three rings with a total of 32 skyrmions. Two 5-7 dislocations are indicated by arrows in Fig. S8(b). When the sample is tilted between -3° and +3°, the position of the dislocations changes from the edges to the corners of the pentagon. At an intermediate tilt of 0°, the outer skyrmion ring at $n = 3$ appears diffuse along the circular direction because the lattice wobbles between the two configurations. On the other hand, the skyrmions of the inner rings stay sharp. In Fig. S8(c), the position of the skyrmions observed at +3° and -3° is indicated by blue and red circles. It can be observed that switching between the two configurations involves a displacement along the circular direction of most of the skyrmions of the outer ring, which can then explain its diffuse appearance at 0°.

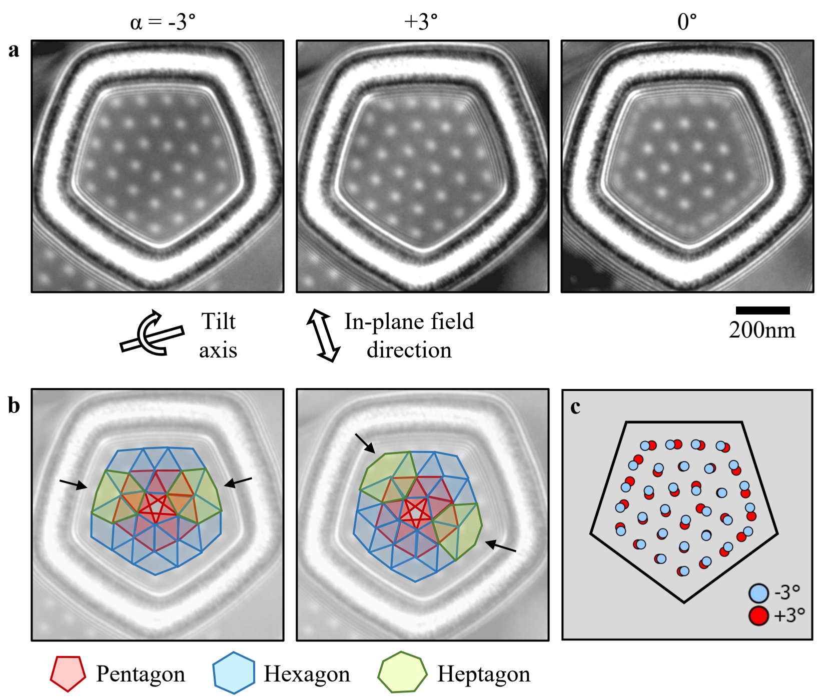

Figure S8: **Skyrmions mobility around a disclination.** (a) Fresnel images of a skyrmion lattice with $S = 32$ skyrmions in a pentagon-shaped sample obtained at 220 K with a defocus of 500 µm, in the presence of an external magnetic field of 230 mT and at different tilt angles $\alpha = -3°, +3°$, and 0°. (b) Images obtained at -3° and +3° overlaid with pentagons, hexagons and heptagons. (c) Positions of the skyrmions in the two tilted images represented by blue and red dots.

Supplementary Information 8: Influence of the thickness of the FIB-damaged layer

To understand the influence of the FIB-damaged layer at the surfaces of the lamella, we performed micromagnetic simulations of a pentagon-shaped sample with 16 skyrmions while varying the thickness of the damaged layers t_{dmg}. Fig. S9(a-f) shows the magnetization in the sample and the corresponding magnetic phase images ϕ_{mag} where t_{dmg} was varied between 0 and 32 nm. With increasing thickness of the damaged layer, the diameter of the skyrmions shrinks near the surfaces (b-d), which is related to the absence of DMI in the damaged regions (see Methods in the main article). This effect progressively distorts the skyrmions, ultimately transforming them into dipole strings [2] – skyrmions that are terminated on both sides by Bloch points. The transformation first affects the central skyrmion of the disclination (e) and subsequently the surrounding skyrmions (f). As a consequence, the associated phase shift of the dipole string states is significantly reduced compared to that of skyrmions, as shown by the radial profiles in Fig. S9(g). For comparison, an experimental profile (dashed line) is also included in Fig. S9(g). Its relatively large phase shifts confirm that the experimentally observed objects remain skyrmionic, even at the center of the disclination, implying that the thickness of the damaged layers is insufficient to induce a transition into dipole strings.

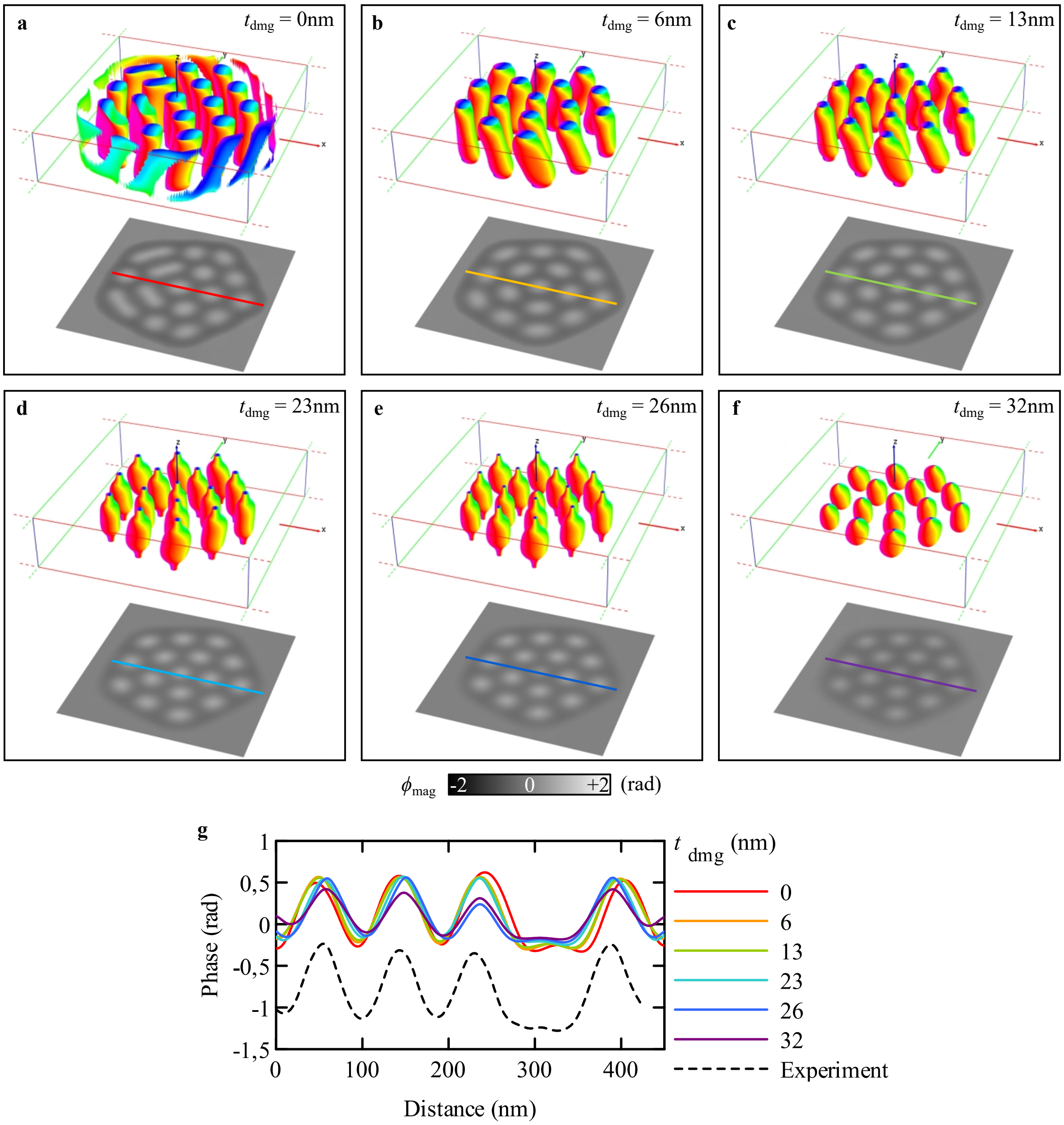

Figure S9: **Influence of the thickness of the FIB-damaged layer.** (a-f) Magnetization in a pentagon-shaped sample represented by the isosurface $m_z = 0$. Each image corresponds to the same sample shape and size but different thicknesses of the amorphous FIB-damaged surface layer: (a) $t_{\text{dmg}} = 0$ nm, (b) 6 nm, (c) 13 nm, (d) 23 nm, (e) 25 nm, and (f) 32 nm. The corresponding magnetic phase images ϕ_{mag} are shown below each model. (g) Phase profiles extracted from the images in (a-f) along the marked lines. An experimental profile (black dashed line) is included for comparison and is vertically offset for clarity.

Supplementary Information 9: Geodesic nudged elastic band (GNEB) script

```
//*** Demagnetizing kernel calculation script ***//

//Discretization
nx := 256;  ny := 256;  nz := 64;   noi := 15;
// Material parameters
Ms := 120e3; Msat = Ms
LD := 70.0e-9; dx := 2.12e-9; dz := 2.12e-9;
dx = dx * 0.95
L := nx*dx; Lz := dz*nz;

SetMeshGNEB(nx,ny,nz,noi,dx,dx,dz,0,0,0, 0, 0)
EnableDemag = true
MaxIter = 1         // Maximal number of iterations
VPOminimize()       // run VPO
```

```
//*** Minimum energy path calculation script ***//

//Discretization
nx := 256; ny := 256; nz := 64; noi := 15;
Ms := 120e3; Msat = Ms
LD := 70.0e-9; dx := 2.12e-9; dz := 2.12e-9;
dx = dx * 0.95
L := nx*dx; Li := dz*nz; Lz := Li*noi;
SetMeshGNEB(nx,ny,nz*noi,noi,dx,dx,dz,0,0,0, 0, 1)

EnableDemag = true
A := 4.75e-12;      //Aex = A;
D := 4.0 * pi * A / LD; //Dbulk = D;

//dead layer thickness
dl := 24e-9
for i:=0; i<noi; i++{
  rzc := i*Li-0.5*Lz+0.5*Li; //center of the domain of each image
  defregion(1, zrange(rzc - (0.5*Li-dl),rzc + (0.5*Li-dl)))
  defregion(0, zrange(rzc - 0.5*Li, rzc - (0.5*Li-dl)))
  defregion(0, zrange(rzc + (0.5*Li-dl),rzc + 0.5*Li ))
}

//construction of pentagon shape
num := 5 //number of sides
fc  := 2.0*pi/num
xc  := cos(fc); yc  := sin(fc)

x_c := -1.311338
y_c := -0.952743
R_c := 2.5

l0 := 2.0*dl/L
```

```
lc := 1.0-l0;
xl := lc*cos(fc)
yl := lc*sin(fc)

for ix := 0; ix < nx; ix++{
  for iy := 0; iy < ny; iy++{
    rx := -1.0 + 2.0*(ix+0.5)/nx
    ry := -1.0 + 2.0*(iy+0.5)/ny
    ri := sqrt(rx*rx + ry*ry)
    fi := atan2(-ry,rx);
    if fi<0{
      fi = fi + 2.0*pi;
    }
    if fi>fc{
      fi = fi - Floor(fi/fc)*fc
    }
    x0 := ri*cos(fi) - x_c;
    y0 := ri*sin(fi) - y_c;

    r0 := sqrt(x0*x0 + y0*y0)
    cond1 := (r0 <= R_c)
    cond1 = (cond1) && (ri <= 0.98)
    cond2 := (r0 <= R_c-2.0*dl/L)
    cond2 = (cond2) && (ri <= (1.0-2.0*dl/L)*0.98)

    if(!cond1){//non-magnetic
      for iz := 0; iz < nz*noi; iz++{
        DefRegionCell(255, ix, iy, iz);
      }
    }else if (cond2){
      for iz := 0; iz < nz*noi; iz++{
        if(Regions.GetCell(ix,iy,iz) != 0){
          DefRegionCell(1, ix, iy, iz);
        }
      }
    }else{//dead layer on sides
      for iz := 0; iz < nz*noi; iz++{
        DefRegionCell(0, ix, iy, iz);
      }
    }
  }
}
//Exchange, DMI and Zeeman
Aex.setregion(1, A)
Aex.setregion(0, A)
Aex.setregion(255, 0)
NoDemagSpins.SetRegion(255, 1)

Dbulk.setregion(1, D)
Dbulk.setregion(255, 0.0)
Dbulk.setregion(0, 0.0)

Th := -5.0*pi/180.0
Fh := -18.0*pi/180.0
Bh := 0.23
```

```
B_ext.setregion(1, vector(Bh*sin(Th)*cos(Fh), Bh*sin(Th)*sin(Fh), Bh*cos(Th)))
B_ext.setregion(0, vector(Bh*sin(Th)*cos(Fh), Bh*sin(Th)*sin(Fh), Bh*cos(Th)))
B_ext.setregion(255, vector(0, 0, 0.0))

// m.LoadFile("path_0.ovf") // for Th :=  0.0
m.LoadFile("path_m.ovf")  // for Th :=  -5.0*pi/180.0
// m.LoadFile("path_p.ovf") // for Th :=  5.0*pi/180.0

save(m)               //save initial state
SavePath(m, noi)
//GNEB relaxation parameters
k_force =  1.0e2    // spring force constant
MaxIter = 1e7       // Maximal number of iterations
WritingIter = 100   // how often write to txt file0
MaxForce = 5e-10    // tolerance for forces
stepsize = 3e-2     // step size in VPO method
VPOminimize()       // run VPO
save(m)             // save final state
SavePath(m, noi)
```

References

[1] Overwijk, M. H. F., van den Heuvel, F. C. & Bulle-Lieuwma, C. W. T. Novel scheme for the preparation of transmission electron microscopy specimens with a focused ion beam. *Journal of Vacuum Science & Technology B: Microelectronics and Nanometer Structures Processing, Measurement, and Phenomena* **11**, 2021–2024 (1993). URL `https://doi.org/10.1116/1.586537`.

[2] Savchenko, A. S. *et al.* Diversity of states in a chiral magnet nanocylinder. *APL Materials* **10**, 061110 (2022). URL `https://doi.org/10.1063/5.0097650`.